Journal of Materials Chemistry A

PAPER

Cite this: J. Mater. Chem. A, 2018, 6, 14867

Diagnosis of failure modes for all-solid-state Li-ion batteries enabled by three-electrode cells†

Young Jin Nam,[ab] Kern Ho Park,[a] Dae Yang Oh,[ab] Woo Hyun An[a] and Yoon Seok Jung *[a]

Received 16th April 2018
Accepted 3rd July 2018

DOI: 10.1039/c8ta03450h

rsc.li/materials-a

Bulk-type all-solid-state Li-ion batteries have emerged as the enabler to achieve better safety and to use Li metal negative electrodes for higher energy density. However, all-solid-state half-cells fabricated using In or Li–In counter electrodes (CEs) have been routinely tested to assess working electrodes (WEs) without any verification. Moreover, there have been few reports on the in-depth analysis of all-solid-state full-cells, which is imperative for practical applications. In this work, for the first time, we report novel bulk-type all-solid-state three-electrode cells that enable successful deconvolution and diagnosis of the voltages of positive and negative electrodes even for cells having thin solid electrolyte (SE) layers. In the first case study, that of Sn/Li–In half-cells, earlier termination of Li–In CEs than Sn WEs, which results in unexpectedly low capacity, is measured. This problem is solved by percolating Li–In with SEs. For the second case, namely, that of $LiNi_{0.6}Co_{0.2}Mn_{0.2}O_2$/graphite full-cells having only 50–60 μm-thick SE layers (which are fabricated by a scalable wet-slurry process), internal short circuits by penetrating growth of Li metal during charging at high C-rates are revealed for the first time. Further, a unique dischargeability to 0 V for $LiNi_{0.6}Co_{0.2}Mn_{0.2}O_2$/graphite or $LiNi_{0.6}Co_{0.2}Mn_{0.2}O_2$/Si–C full-cells is described.

Introduction

Since the first commercialization of lithium-ion batteries (LIBs) in the early 1990s, their energy density has been more than doubled as a result of extensive engineering and materials chemistry research.[1,2] However, further improvements face serious safety concerns. Engineering efforts towards thinning the separators (≤10 μm) are offset by greater vulnerability toward internal short circuits (ISCs).[3,4] Although the use of Li metal for negative electrodes had been abandoned because of its catastrophic safety issue, without it, a significant increase in energy density is hard to achieve.[5–7] All-solid-state lithium or lithium-ion batteries (ASLBs) using inorganic solid electrolytes (SEs) have emerged to solve the safety concerns originating from the use of flammable organic liquid electrolytes (LEs) and also to enable the use of Li metal.[6,8–13] Composite-structured bulk-type ASLBs are especially attractive in terms of their potential for high energy density and scalable fabrication.[9,14–17] Several promising performances of bulk-type all-solid-state Li- and Na-ion batteries employing extremely conductive (10^{-3} to 10^{-2} S cm^{-1} at room temperature) and deformable sulfide SE materials have brought explosive interest in this field.[6,9,14,15,17–25]

Reliable electrochemical test protocols are a prerequisite in R&D for advanced materials and devices for batteries. Li metal is routinely used as a counter electrode (CE) and simultaneously as a reference electrode (RE) in the half-cells for conventional LIBs because of its constant voltage even at high current densities. However, interpretation of the performances of working electrodes (WEs) is hindered by Li metal electrodes in some cases, such as where the usage of Li metal is heavy in terms of the number of cycles or apparent capacity,[26,27] and/or where complicated chemistry results in too thick passivation layers on Li metal.[5,26] Contrary to the anticipated compatibility of SEs with Li metal, recent reports on this matter unveiled serious challenges: not only a deteriorating chemical reaction of SEs with Li metal, dependent on the composition of the SEs,[28] but also the penetrating growth of Li metal into the defects of SE structures.[9,29–32] This must be the reason why In or Li–In, not Li metal, has been mostly used as the counter and reference electrode in the half-cells for ASLBs.[9,14,15,17,18,28] Since the reaction of In with Li^+ ions proceeds *via* a two-phase reaction ($In + Li^+ + e^- \rightarrow LiIn$) with a flat voltage plateau at 0.62 V (*vs.* Li/Li^+),[33] it serves as a good RE. However, its significant contribution to the kinetic behavior of all-solid-state half-cells has not been evaluated yet, deterring reliable interpretation of WEs. In a previous study regarding the impedance analysis of $LiCoO_2$/In all-solid-state cells, it was observed that interfacial resistance in the low-frequency region, which was assigned to the In-SE interfacial one, became huge at the end of discharge.[34] In particular, the reliability of In or Li–In as counter and reference

[a]Department of Energy Engineering, Hanyang University, Seoul 04763, Republic of Korea. E-mail: yoonsjung@hanyang.ac.kr

[b]School of Energy and Chemical Engineering, Ulsan National Institute of Science and Technology (UNIST), 50 UNIST-gil, Ulsan 44919, Republic of Korea

† Electronic supplementary information (ESI) available. See DOI: 10.1039/c8ta03450h

electrodes in all-solid-state half-cells must be carefully evaluated when alternative electrode materials (*e.g.*, Sn, Si, and S) are tested because their capacities far exceed the usage ranges of the CEs for the cases using conventional electrode materials (*e.g.*, $LiCoO_2$ and graphite (Gr)).

In this regard, the development of reliable all-solid-state three-electrode cells that allow deconvolution of the signals for positive and negative electrodes is imperative. Three-electrode cells using LEs are fabricated by placing REs in between positive and negative electrodes[35] or close to the side edge of sandwiched positive and negative electrodes (Swagelok cell).[36] For thin-film-type ASLBs fabricated by vacuum deposition, few reports about three-electrode cells using Li metal as the RE are found.[37] Unfortunately, the unique fabrication protocol for bulk-type all-solid-state cells, which is based on cold-pressing under high pressures (hundreds of MPa) and the use of a pelletizing mold, makes the design of bulk-type all-solid-state three-electrode cells extremely challenging. Moreover, while ≥500 μm-thick SE separating layers have been frequently used for conventional tests of bulk-type ASLBs, from a practical perspective, the thickness must be reduced to tens of micrometers.[15,38,39] This strictly restricts the application of the conventional design for LE-based three-electrode cells to all-solid-state three-electrode cells.

Here, we report, a novel bulk-type all-solid-state three-electrode cell with a configuration of RE/SE/WE/SE/CE, which allows precise separation of voltages for positive and negative electrodes despite using thin (tens of micrometers) SE layers. The first instance of Sn/Li–In half-cells shows that the overall capacity is limited by the Li–In CEs, not by the Sn WEs, which is solved by the use of Li–In-SE CEs. The second instance involves $LiNi_{0.6}Co_{0.2}Mn_{0.2}O_2$ (NCM)/Gr full-cells assembled using sheet-type electrodes and thin (50–60 μm) SE layers by the scalable wet-slurry method. Soft ISCs by penetrating growth of Li metal into the SE layers during charge at high C-rates are evidenced. The unique durability of the all-solid-state full-cells upon discharge to 0 V is also analyzed.

Results and discussion

Sn/Li–In half cells

Sn could be a suitable negative electrode material to achieve high energy density for ASLBs because of its high theoretical capacity (992 mA h g^{-1}), metallic properties, and ductility, which allows intimate contact with SEs by simple cold-pressing.[40,41] However, we found that the capacity of Sn in Sn/Li–In half-cells is unexpectedly low and strongly dependent on the loading amount (Fig. 1); the first-cycle lithiation (or discharge) capacity of 534 mA h g_{Sn}^{-1} for 4 $mg_{electrode}$ cm^{-2} decreases to only 307 mA h g_{Sn}^{-1} for 10 $mg_{electrode}$ cm^{-2}. These values are far smaller than that for the conventional Sn/Li half-cells using LEs (958 mA h g_{Sn}^{-1}, Fig. S1, ESI†). Note that an excessive amount of Li–In (nominal composition of $Li_{0.5}In$) was employed for CEs to accommodate the full lithiation–delithiation of Sn WEs (see the Experimental section for details). Interestingly, the overall capacity difference in all-solid-state Sn/Li–In cells for discharge originates mainly from the capacities in the voltage region

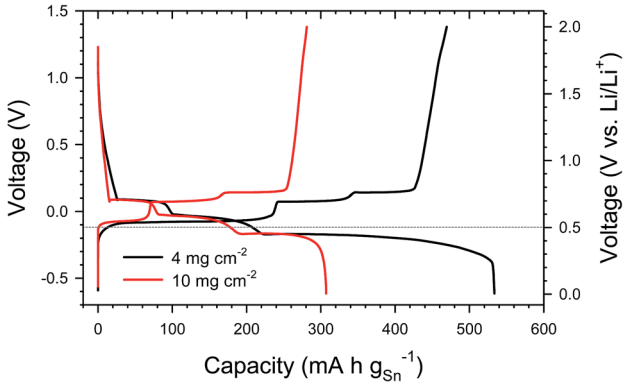

Fig. 1 First-cycle discharge–charge voltage profiles for Sn/Li–In all-solid-state cells with two different electrode mass loadings.

below 0.5 V (*vs.* Li/Li^+) while the capacities in the two-plateau regions above 0.5 V (*vs.* Li/Li^+) (180–220 mA h g_{Sn}^{-1}) are similar to that for the Sn/Li half-cell using LEs (at the second cycle). This observation led us to suspect that the overall capacity may be more affected by Li–In CEs than by Sn WEs.

The first design of an all-solid-state three-electrode cell (referred to as 'cell-1') is illustrated in Fig. 2a, in which the RE is in contact with the side of the SE layer. Unfortunately, this design requires too thick (at least 1 mm thick) SE layers. This problem was solved by contacting the RE on the backside of the WE through an additional SE layer as illustrated in Fig. 2b (referred to as 'cell-2'). The discharge–charge voltage profiles of Sn (4 $mg_{electrode}$ cm^{-2})/Li–In half-cells for cell-1 and cell-2 at different current densities are shown in Fig. 2c. Cell-1 shows lower capacity and poorer rate capability than cell-2. This is attributed to the higher resistance of the thicker SE layer in cell-1 (2.2 mm) as compared with cell-2 (730 μm). Fig. 2d presents the separated discharge–charge voltage profiles at 0.045 mA cm^{-2} for Sn WEs and Li–In CEs *vs.* Li/Li^+ (WE/RE and CE/RE, respectively) as well as the ones for Sn WEs with respect to Li–In CEs (WE/CE). As suspected, the overall discharge is ended by termination of Li–In CEs, not Sn WEs. Although the discharge cut-off voltage for Sn/Li–In cells was set to be 0 V *vs.* Li/Li^+ (or −0.62 V for the WE with respect to the CE), in reality the terminal voltages for Sn electrodes are much higher than 0 V *vs.* Li/Li^+ (0.43 and 0.36 V *vs.* Li/Li^+ for cell-1 and cell-2, respectively) because of early termination of discharge by Li–In CEs. This result clearly indicates that the unexpectedly low capacities of all-solid-state Sn/Li–In half-cells (Fig. 1) come from the poor capacity or kinetics of Li–In CEs, not Sn WEs. It is confirmed that, when using the Li–In RE, calibration of voltages for the WE and CE in the scale of *vs.* Li/Li^+ by adding 0.62 V shows a marginal difference, compared with the case when using the Li metal RE (Fig. S2, ESI†).

Following the afore-learned lesson, we attempted to enhance the usage of Li–In CEs by percolating with SE powder. All-solid-state half-cells for Sn (10 $mg_{electrode}$ cm^{-2}), using three different CEs by varying the weight fraction of SE (0, 10, and 20 wt% which correspond to approximately 0, 26, 44 vol%, respectively), were fabricated. Their discharge–charge voltage profiles at different current densities are compared in Fig. 3a. The discharge capacity

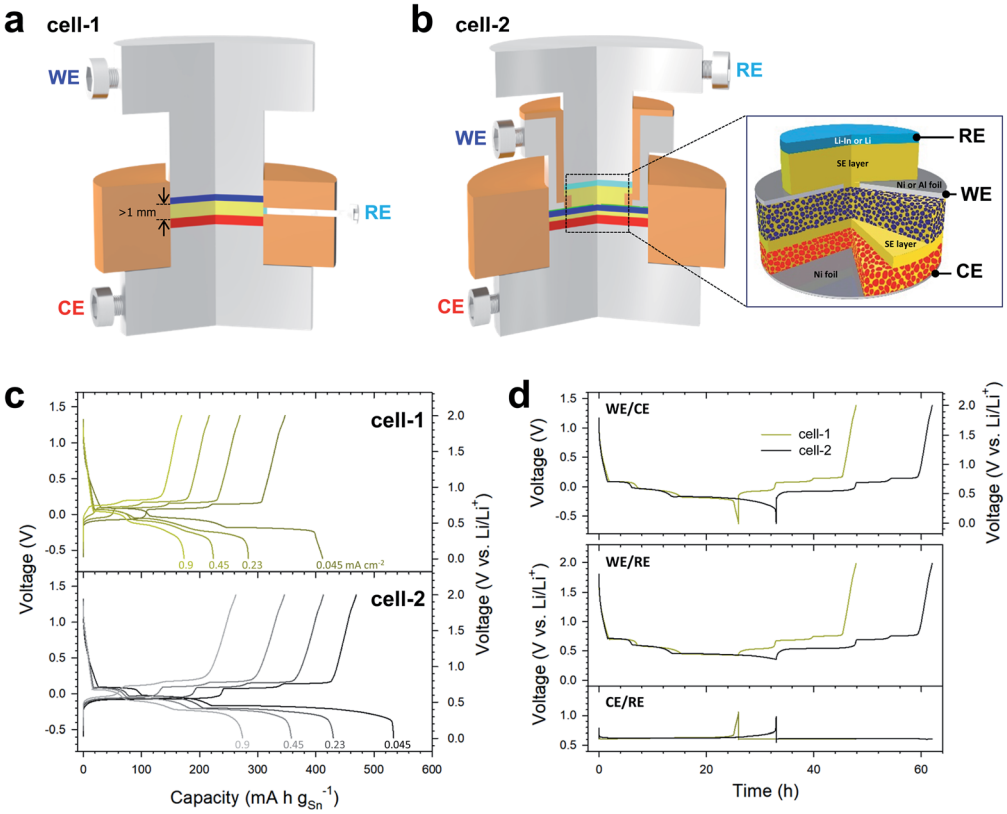

Fig. 2 Results for two different types of all-solid-state three-electrode cells. Schematics of all-solid-state three-electrode cells of (a) type 1 (referred to as "cell-1") and (b) type 2 (referred to as "cell-2"). Polymeric binders (NBR) and carbon additives (Super C65) are not shown in the diagram (WE and CE) for simplicity (b). (c) Discharge–charge voltage profiles for Sn/Li–In all-solid-state three-electrode cells at different current densities. (d) Discharge–charge voltage profiles of each electrode for Sn/Li–In all-solid-state three-electrode cells at 0.045 mA cm^{-2}.

at 0.11 mA cm^{-2} is dramatically increased to 652 mA h g_{Sn}^{-1} with 10 wt% SE in the CE, and reaches 689 mA h g_{Sn}^{-1} with 20 wt% SE, which approaches the value for the LE-cell (958 mA h g_{Sn}^{-1}, Fig. S1, ESI†). The enhancement in capacity at higher current densities is more dramatic with 20 wt% SEs than with 10 wt% SEs. The separated discharge–charge voltage profiles at 0.11 mA cm^{-2} for Sn WEs and Li–In(-SE) CEs *vs.* Li/Li^+ in Fig. 3b undoubtedly reveal that the lithiation (or discharge) of Sn WEs close to 0 V (*vs.* Li/Li^+) is enabled by the use of Li–In-SE CEs. Also, the dramatic decrease in termination voltage from 1.07 V (*vs.* Li/Li^+) for the SE-free Li–In CE to 0.72 and 0.71 V (*vs.* Li/Li^+) for the Li–In-SE CEs with 10 and 20 wt% SE, respectively, reflects the extended usage of Li–In by the percolated SEs. The terminal voltages of Li–In or Li–In-SE CEs, varying with current densities, are plotted in Fig. 3c (the full voltage profiles at various current densities are provided in Fig. S3, ESI†). Consistently, increasing amounts of SE in CEs (20 wt% SE) result in lower terminal voltages, especially at higher current densities.

After the all-solid-state Sn/Li–In and Sn/Li–In-SE (20 wt% SE) half-cells were fully discharged down to −0.62 V (corresponding to the target cut-off voltage of 0 V *vs.* Li/Li^+ for Sn WE), the disassembled CEs were subjected to analysis using time-of-flight secondary ion mass spectrometry (TOF-SIMS). Cross-sectional field emission scanning electron microscopy (FESEM) images and their corresponding energy dispersive X-ray spectroscopy (EDXS) elemental maps for the CEs are provided. (Fig. S4, ESI†) The concentration distribution of Li^+ ions in the cross-sectioned SE-free Li–In and Li–In-SE CEs is shown in Fig. 4a and b, respectively. The thickness of the Li-depleted layer is estimated to be ~50 μm for the Li–In CE (Fig. 4a). In stark contrast, for the Li–In-SE CE, the Li-depleted or deficient signals are distributed in much deeper regions. From this observation, schematic diagrams for cross-sectional views of Li–In and Li–In-SE CEs are illustrated in Fig. 4c and d, respectively. For the Li–In CE, upon discharge of Sn/Li–In half-cells, the Li-depleted indium layer is formed at the top of the CE, impeding further movement of Li^+ ions from the inner regions of Li–In to the SE layer, which results in early termination of the cells. In contrast, for Li–In-SE CEs, utilization of Li^+ ions from much deeper regions of CEs could be facilitated by the aid of percolated SEs. In short, apart from our success in developing the first reliable bulk-type all-solid-state three-electrode cells, the development of Li–In-SE CEs provides a reliable test protocol for all-solid-state half-cells that is much less affected by high-capacity WEs and high current density.

NCM/Gr full-cells

The second test vehicle for all-solid-state three-electrode cells is wet-slurry-fabricated NCM/Gr full-cells having thin SE layers. A cross-sectional FESEM image of the full-cell and its

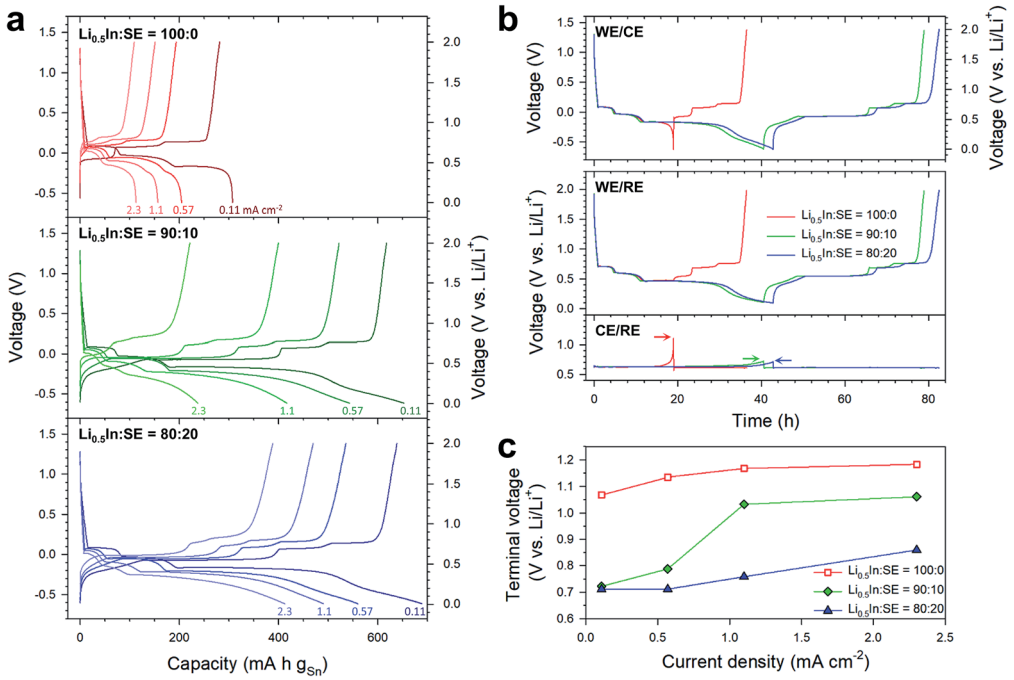

Fig. 3 Electrochemical results for Sn/Li–In(-SE) all-solid-state three-electrode cells with different CEs (counter electrodes). (a) Discharge–charge voltage profiles (WE *vs.* CE) for the cells with different CEs where three different weight ratios of $Li_{0.5}In$/SE were used. The numbers indicate the current density in mA cm^{-2}. (b) Discharge–charge voltage profiles for each electrode at 0.11 mA cm^{-2}. The arrows indicate the terminal voltage of CEs ($Li_{0.5}In$ or $Li_{0.5}In$-SE) upon discharge (delithiation for CEs). (c) Terminal voltage for CEs ($Li_{0.5}In$ or $Li_{0.5}In$-SE) upon discharge (delithiation for CEs) as a function of current density, which is plotted from the data in (b) and Fig. S3, ESI†.

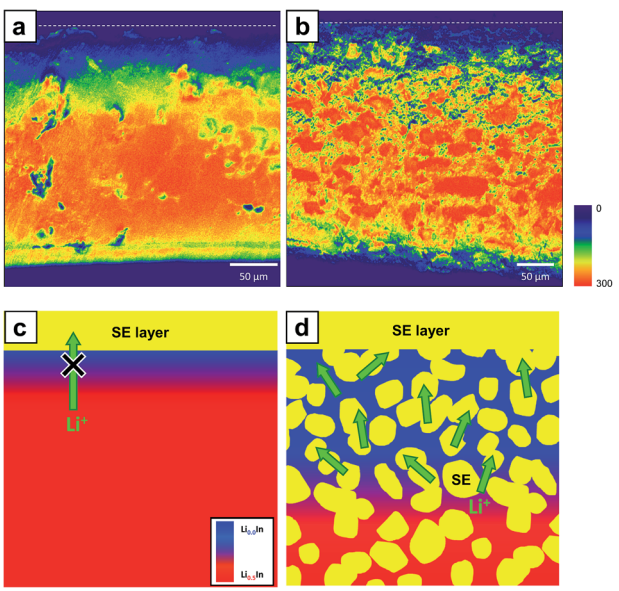

Fig. 4 Results for the concentration of Li^+ ions in cross-sectioned CEs ($Li_{0.5}In$ or $Li_{0.5}In$-SE with 80 : 20 weight ratio) for Sn/Li–In(-SE) all-solid-state cells. Cross-sectional TOF-SIMS maps of Li^+ ions for (a) $Li_{0.5}In$ and (b) $Li_{0.5}In$-SE CEs. The dashed lines indicate the outer surface of CEs. A scale bar with the maximum ion counts in a.u. is displayed in the right of (b). Schematics showing the concentration of Li^+ ions in cross-sectioned (c) $Li_{0.5}In$ and (d) $Li_{0.5}In$-SE CEs.

corresponding EDXS elemental maps clearly show a 50–60 μm thick SE layer in between NCM and Gr electrodes without any noticeable mechanical failure (Fig. S5, ESI†). In NCM/Gr three-electrode cells, the upper SE layer in between the RE and the WE is in contact with the NCM electrode layer through a tiny hole (~1 mm^2) where the Al current collector is removed, as illustrated in Fig. 2b. Note that the experimental conditions for the full-cells are realistic for practical applications in terms of the mass loadings (23 and 14 $mg_{electrode}$ cm^{-2} for NCM and Gr electrodes, respectively) and the thickness of the SE layer (50–60 μm).[15,39,42] The NCM/Li–In and Gr/Li–In-SE (20 wt% SE) half-cells showed first-cycle reversible capacities of 149 and 310 mA h g^{-1}, respectively, at 0.1C (Fig. S6, ESI†).

Fig. 5a shows charge–discharge voltage profiles for the NCM/Gr full-cell at different C-rates and their corresponding differential capacity curves. The discharge capacity of the full-cell is 137 mA h g_{NCM}^{-1} at 0.1C. As the C-rate is increased, the data show increased polarization and consequently decreased capacities (*e.g.*, 82 mA h g_{NCM}^{-1} at 1C), which is not surprising. However, abnormal behaviors are observed for the charge voltage curves starting at 0.5C: plateaus in the high voltage regions beginning at ~4.1 V (indicated by the lines in red), corresponding to the sharp peaks in the differential capacity plots. The separated voltage profiles for NCM and Gr electrodes *vs.* Li/Li^+ at 0.1C and 1C, measured from three-electrode cells, are plotted in Fig. 5b (the full voltage profiles at various C-rates are also provided in Fig. S7, ESI†). Starting at 1C, charging of the Gr electrode proceeds below 0 V (*vs.* Li/Li^+). This would

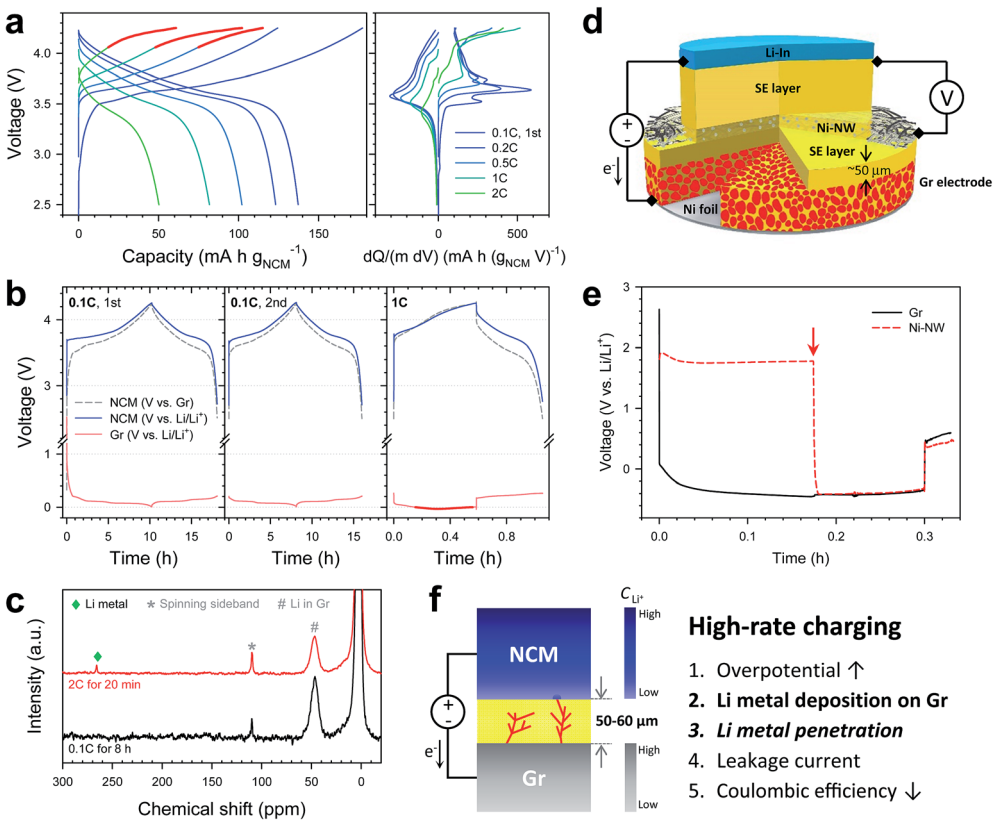

Fig. 5 Results for NCM/Gr all-solid-state three-electrode cells employing thin SE layers (50–60 μm), suffering from ISC by penetrating growth of Li metal. (a) Charge–discharge voltage profiles and the corresponding differential capacity plots at different C-rates. Note the abnormal plateaus plotted in red during charge at high C-rates. (b) Transient charge–discharge voltage profiles for each electrode at different C-rates. Note the voltage region of Gr, which is lower than 0 V (*vs.* Li/Li$^+$) at high C-rate, 1C, shown by a thick red line. (c) ^{7}Li MAS-NMR spectra for the mixtures of SE layers and Gr electrodes collected from the Gr electrodes after lithiation at 0.1C or 2C. The corresponding voltage profiles are provided in Fig. S9, ESI†. (d) Schematic illustrating Gr/Ni-NW/Li–In all-solid-state three-electrode cells and (e) the corresponding transient charge–discharge voltage profiles at 2C for Gr and Ni-NW electrodes. While the current flows between Gr and Li–In electrodes, the voltage of Ni-NW electrodes was measured to detect the ISC. Polymeric binders (NBR) are not shown in the diagram (Gr electrode) for simplicity (d). (f) Schematic showing the ISC induced by the penetration of Li metal for NCM/Gr all-solid-state cells during charge at high C-rates.

inevitably lead to deposition of Li metal on the surface of Gr.[43–45] One more interesting abnormal feature is much lower coulombic efficiency values at high C-rates (≥0.5C) than those at low C-rates (Table 1). 99.0% coulombic efficiency at 0.2C is drastically decreased to 88.7, 80.3, and 82.5% at 0.5C, 1C, and 2C, respectively. Consistently, NCM/Li all-solid-state cells show abnormal behaviors similar to the NCM/Gr full-cells: a plateau at the later stage of charge (delithiation for the NCM electrode and Li plating for the Li metal electrode) at high C-rates and the corresponding excessive charge capacity (Fig. S8, ESI†). These observations suggest soft ISCs caused by penetrating growth of Li metal through the SE layers.[3,9,13,31,43–45] In order to verify the deposition of Li metal in the Gr electrodes for all-solid-state cells, *ex situ* ^{7}Li magic angle spinning nuclear magnetic resonance (MAS-NMR) measurements were carried out for the mixture samples of Gr electrodes and SE layers in contact with the Gr electrodes from the Gr/Li–In all-solid-state cells after lithiating the Gr electrodes at two different C-rates of 0.1C (for 8 h) or 2C (20 min) (Fig. S9, ESI†). The spectrum of the sample collected from the cell run at 2C shows clear evidence of the formation of metallic Li at 264 ppm (denoted '◆', Fig. 5c).[46] In sharp contrast, the spectrum for the case of the lower C-rate

Table 1 Coulombic efficiency for NCM/Gr all-solid-state full-cells

Thickness of the SE layer [μm]	Characteristics	0.1C (1st)	0.1C (2nd)	0.2C (4th)	0.5C (9th)	1C (14th)	2C (19th)
50–60	Discharge capacity [mA h g^{-1}]	177	141	124	115	102	61
	Charge capacity [mA h g^{-1}]	137	137	123	102	82	50
	Coulombic efficiency [%]	77.3	97.5	99.0	88.7	80.3	82.5
730	Discharge capacity [mA h g^{-1}]	184	145	130	103	76	42
	Charge capacity [mA h g^{-1}]	146	145	130	103	76	42
	Coulombic efficiency [%]	79.2	99.8	100.0	99.8	99.7	99.5

(0.1C) is free from any signals of metallic Li. Further, unique all-solid-state three-electrode cells of Gr/Ni-coated nonwoven (Ni-NW)/Li–In were prepared as an attempt to directly detect penetrating growth of Li metal through the SE layers (Fig. 5d). The SEs could be impregnated into the porous structures of the Ni-NW electrode, being interconnected to provide good ionic conduction pathways through the Ni-NW electrode.[38] The lithiation current of 2C for the Gr electrode was applied between Gr and Li–In electrodes while the voltage of the Ni-NW electrode with respect to the Li–In electrode was measured. Again, the C-rate of 2C is high enough to result in a charging voltage of Gr electrodes below 0 V (*vs.* Li/Li^+) in the NCM/Gr full-cells and the corresponding abnormal behaviors of high voltage plateaus (Fig. 5a) and low coulombic efficiencies (Table 1). The voltage of the Ni-NW electrode remains constant at ~1.8 V (*vs.* Li/Li^+) up to 0.17 h (Fig. 5e). However, it abruptly falls to the voltage close to the one for the Gr electrodes. This result clarifies the electrical connection (or ISC) between Ni-NW and Gr electrodes, which must be attributed to the penetrating growth of Li metal through the SE layers. In short, the deposition of metallic Li in Gr electrodes at high C-rate and the ISC caused by penetrating growth of Li metal through the SE layers were unprecedentedly evidenced from the results of ^7Li MAS-NMR and the unique Gr/Ni-NW/Li–In all-solid-state three-electrode cells.

From the complementary analysis results so far, the penetrating growth of Li metal in the NCM/Gr all-solid-state full-cells and its effect on the abnormal electrochemical behaviors are illustrated in Fig. 5f. Once any ISCs are made by the penetrating Li metal, NCM being in touch with Li metal will be chemically lithiated by consuming the as-contacted Li metal, which is the opposite direction to charge and causes leakage of current. Consequently, significant imbalance in the amount of charge and discharge through the external circuits (or low coulombic efficiency) is observed. The results for NCM/Gr full-cell having conventional thicker SE layers (730 μm) are also compared (Fig. S10, ESI†). The discharge of Gr electrodes under 0 V (*vs.* Li/Li^+) is still observed, indicating the possible deposition of Li metal on Gr. However, the abnormal behaviors of the high-voltage plateaus (Fig. 5a) and the low CE values at high C-rates (Table 1) are not seen for the case using thicker SE layers. This could be rationalized by much less possibility of ISC because of approx. ten times longer distances for Li metal to penetrate through.

It is worth noting that no significant changes in mechanical integrity for the composite NCM and Gr electrodes were observed after cycling (Fig. S11, ESI†). It is considered that the applied pressure (74 MPa) during the operation of all-solid-state cells would deform the SEs having low Young's modulus of 20–30 GPa,[47] maintaining the integrity of the composite electrodes. However, severer test conditions, such as extended cycling and less applied pressure, may cause mechanical failure of ASLBs, which will be the subject in the future work.

Once activated by formation cycles in the manufacturing processes, conventional LIBs using LEs must not be discharged to 0 V because of permanent failure of the cells by dissolution of Cu current collectors for negative electrodes, which experience high voltages above 3 V (*vs.* Li/Li^+).[48] Therefore, careful management in discharge is necessary to guarantee the health and safety of LIBs.[48] For the case of ASLBs, Cu might not be used as the current collector because of its chemical reactivity with sulfide materials (Ni foils were used for negative electrodes in this work). Even if the Cu current collector could be used for ASLBs, there is no dissolution issue. In this regard, the durability of ASLBs upon discharge to 0 V needs to be assessed.

Another interesting feature found in the behavior of the all-solid-state NCM/Gr full-cell in Fig. 5b is the balance in the utilization of positive and negative electrodes. The overall first-cycle discharge is ended by full lithiation of NCM, not by full delithiation of Gr, which is opposite to the case for conventional LIBs using LEs.[35] This unique feature stems from the lower first-cycle coulombic efficiency of NCM (79.1%) in contact with SEs than that of Gr (92.5%) (Fig. S6, ESI†). For systematic assessment, a NCM/Si–C full-cell, where the Si–C electrode shows much lower first-cycle coulombic efficiency (66.7%) than Gr or NCM electrodes, is compared. After normal charge–discharge for three cycles (2.50–4.25 V and 1.20–4.25 V for NCM/Gr and NCM/Si–C, respectively), the NCM/Gr and NCM/Si–C full-cells were subjected to discharge to 0 V at constant current and the

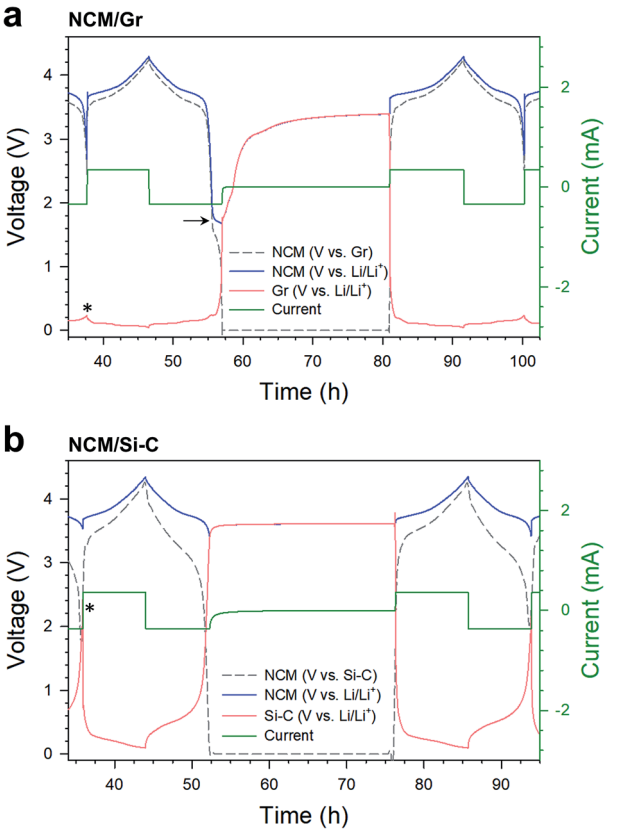

Fig. 6 Results for NCM/Gr and NCM/Si–C all-solid-state three-electrode cells discharged to 0 V. Transient charge–discharge voltage profiles for each electrode for (a) NCM/Gr and (b) NCM/Si–C cells during discharge to 0 V. Note the higher cutoff voltage for the Si–C electrode in (b) than that for the Gr electrode in (a) (indicated by '*') during normal discharge. Also note the lower terminal voltage for the NCM electrode in the NCM/Gr cell (indicated by an arrow) in (a) than that for the NCM electrode in the NCM/Si–C cell in (b) upon discharge to 0 V.

subsequent constant voltage of 0 V for 24 h. Then, they were cycled in the normal voltage ranges again. The transient voltage profiles during discharge to 0 V are presented in Fig. 6 (the overall transient voltage curves are also shown in Fig. S12, ESI†). As designed, the normal discharge is ended by termination (or full utilization) of the NCM electrode for NCM/Gr and the Si–C electrode for NCM/Si–C (note the terminal voltage for the Si–C electrode is much higher than that for the Gr electrode, as indicated by the sign of '*'). Discharge to 0 V at the following cycle for NCM/Gr leads to an excessive lithiation reaction for the NCM electrode at ~1.8 V (*vs.* Li/Li^+), as indicated by the arrow in Fig. 6a. In contrast, the voltages of NCM electrodes for NCM/Si–C remain high above 3 V (*vs.* Li/Li^+) (Fig. 6b). At the subsequent cycles in the normal voltage ranges, unexpectedly, not only NCM/Si–C but also the NCM/Gr full-cell shows no noticeable degradation, as shown in Fig. 6 and S12–14, ESI.† In a recent study for Ni-rich $LiNi_{0.75}Co_{0.25}O_2$, a plateau at 1.75 V (*vs.* Li/Li^+) upon over-discharge was observed, which was assigned as a reversible two-phase transformation without breakdown of the layered host structure by an *in situ* XRD analysis.[49] While clear elucidation on the mechanism for reversible over-discharge of the NCM electrodes for ASLBs upon discharge to 0 V remains, the 0 V dischargeability for ASLBs will offer more flexibility in their management and handling in terms of charge–discharge ranges and less safety concerns (*e.g.*, transportation by airplanes).[48]

Conclusions

In summary, we successfully demonstrated the development of a novel all-solid-state three-electrode cell that enabled diagnosis of failure modes for positive and negative electrodes separately, even for the cells having thin (tens of micrometers) SE layers. For Sn/Li–In half-cells, it was clearly revealed that the overall capacity was limited by the Li–In CEs, not by the Sn WEs, which was attributed to the formation of Li-depleted insulating In layers. This problem was solved by the use of composite Li–In-SE CEs. For NCM/Gr full-cells having thin SE layers (50–60 μm), fabricated by the scalable wet-slurry processes, the soft ISCs due to the penetrating growth of Li metal through the SE layers during charge at high C-rates were reflected by the abnormal plateaus at high voltages, the discharge of Gr electrodes under 0 V (*vs.* Li/Li^+), and the low coulombic efficiencies, and unprecedentedly evidenced by the results of ^{7}Li MAS-NMR and the Gr/Ni-NW/Li–In all-solid-state three-electrode cells. Furthermore, unique durability of NCM/Gr full-cells upon discharge to 0 V was found despite the over-discharge of the NCM electrode. The Li–In-SE CEs developed in this work serve as a reliable test protocol for all-solid-state half-cells. More importantly, the bulk-type all-solid-state three-electrode cells demonstrated in this work are novel and provide a reliable platform for the in-depth interpretation of all-solid-state battery performance. For example, all-solid-state Na-ion batteries, which suffer from the poorer stability of negative electrodes than Li-ion counterparts, could also be analyzed using three-electrode cells.[23,50] The observation of ISC behaviors by the penetrating growth of Li metal for Li-metal-free all-solid-state full-cells is the first time, which is disappointing for the hope in this field but provides new insight into the design of materials (*e.g.*, nano-engineering at grain boundaries) and cells for reliable all-solid-state technology.

Experimental

Preparation of materials

Argyrodite Li_6PS_5Cl SE powder was prepared by mechanical-milling and subsequent heat-treatment. A stoichiometric mixture of Li_2S (99.9%, Alfa Aesar), P_2S_5 (99%, Sigma Aldrich), and LiCl (99.99%, Sigma Aldrich) was ball-milled at 600 rpm for 10 h at room temperature in a ZrO_2 vial with ZrO_2 balls using a planetary ball mill (Pulverisette 7PL; Fritsch GmbH). The resulting powder was heat-treated at 550 °C for 5 h in a sealed fused silica tube. The as-prepared SE powder showed a Li-ion conductivity of 3.0×10^{-3} S cm^{-1} at 30 °C.[36]

Materials characterization

The cross-sectional surfaces of the samples were prepared by polishing at 1.5 kV for 4 h with an Ar ion beam (HITACHI, IM4000). The FESEM images and the corresponding EDXS elemental maps were obtained using an S-4800 (HITACHI). TOF-SIMS analyses were conducted on a TOF SIMS 5 (ION-TOF GmbH, Heisenbergstraβe, Münster). A 25 keV pulsed Bi^+ ion source was employed for analysis and sputtering. The TOF-SIMS imaging areas were 300×300 μm^2 and 450×450 μm^2 for the cross-sectioned Li–In and Li–In-SE CEs, respectively. The base pressure of the analysis chamber was maintained at $<5.0 \times 10^{-10}$ Pa during all analyses. The ^{7}Li MAS-NMR spectra were obtained at 233.12 MHz at a rotor frequency of 25 kHz with 1.2 μs of 90° pulses using an Agilent VNMRS 600 MHz Solid NMR spectrometer with a 1.6 mm HXY Fast MAS probe. Chemical shift for ^{7}Li is referenced to LiCl powder. For the *ex situ* ^{7}Li MAS-NMR measurements, after the Gr electrodes for Gr/Li–In all-solid-state half-cells were lithiated at 0.1C for 8 h or at 2C for 20 min, the Gr electrodes and the SE layers, which were in contact with the Gr electrodes, were carefully collected and subjected to the measurements without exposure to air.

Electrochemical characterization

The Sn electrodes for all-solid-state half-cells were obtained by manual mixing of Sn (99%, 10 μm, Sigma-Aldrich) and SE powder (Li_6PS_5Cl) with a weight ratio of 70 : 30. The wet-slurry-fabricated electrodes were obtained by the following procedure. Slurries were prepared by mixing active materials (NCM or Gr or Si–C powder), SE powder, nitrile-butadiene rubber (NBR), and carbon additives (only for positive electrodes) in anhydrous xylene with the weight ratios of 68.1 : 29.2 : 1.4 : 1.3, 58.6 : 39.1 : 2.3 : 0.0, and 59.4 : 39.6 : 1.0 : 0.0 for the NCM, Gr, and Si–C electrodes, respectively. After the as-prepared slurries were coated on current collectors (Al and Ni foil for the NCM and Gr (or Si–C) electrodes, respectively) using the doctor blade method, the electrodes were obtained by heating at 120 °C and subsequent drying overnight under vacuum. The CEs for the half-cells were fabricated by mixing Li metal (FMC Lithium

Corp.) and In powder (99%, Sigma-Aldrich) with or without SE powder with the target weight ratios using a Thinky mixer at 2000 rpm for 1 min. The amount of $Li_{0.5}In$ or $Li_{0.5}In$-SE CEs was controlled so that the CEs accommodate more than two times higher full capacity for WEs by full lithiation of $Li_{0.5}In$ to LiIn. For example, the amount of Li–In(-SE) CEs for the Sn electrode was set to accommodate a capacity of 959 mA h g_{Sn}^{-1} for WEs. For the fabrication of the Sn/Li–In(-SE) half-cells, the mixed Sn WE and Li–In(-SE) CE powders were spread on the other surfaces of the pre-pelletized SE (Li_6PS_5Cl) layer (150 mg). For fabrication of the NCM/Gr (or NCM/Si–C) full-cells with the thick SE layers, the slurry-prepared electrodes were assembled with pre-pelletized SE layers. For fabrication of the NCM/Gr full-cells with the thin SE layers (50–60 μm), the SE layers were coated directly on the as-formed Gr electrode by the doctor-blade method using a xylene-NBR-based slurry. The np ratios (the areal capacity ratio of negative to positive electrodes) for NCM/Gr and NCM/Si–C full cells were approx. 1.1. For fabrication of three-electrode cells, after the WE/SE/CE assembly for the half-cells or full-cells were pressed at 370 MPa, additional SE layers (120 mg of Li_6PS_5Cl) were put on top of the WEs (Fig. 2b). Finally, the $Li_{0.5}In$ powder or Li metal foil as the RE was put on the top of the SE layer, forming RE/SE/WE/SE/CE, followed by pressing at 74 MPa or 15 MPa, respectively. For the NCM/Gr (or NCM/Si–C) three-electrode cells, a small piece of Al current collectors was carefully removed in order to connect the RE and WE layers through the SE layer as illustrated in Fig. 2b. For the *ex situ* ^{7}Li MAS-NMR measurements, the slurry-fabricated Gr electrodes and 150 mg of Li_6PS_5Cl powder (∼730 μm) as the SE layer were employed. For the Gr/Ni-NW/Li–In all-solid-state three-electrode cells, the slurry-fabricated Gr electrodes were used. The Ni-NW electrode was prepared by depositing Ni on NW using a DC sputtering system (Sorona, SRN-120) at 700 W for 25 min at 10 mTorr under Ar.[35] All the procedures were performed in a polyaryletheretherketone (PEEK) mold (diameter = 1.3 cm) with Ti metal current collectors. All the processes for fabricating the all-solid-state cells were performed in an Ar-filled dry box. The Sn/Li–In(-SE) half-cells, NCM/Gr and NCM/Si–C full-cells were cycled at the target C-rates at 30 °C between 0.0 and 2.0 V, 2.50–4.25 V and 1.20–4.25 V, respectively. All the all-solid-state cells were cycled under 74 MPa. The galvanostatic charge–discharge tests were carried out by applying the current between the WE and CE while the open-circuit voltage of the WE/RE was measured.

Conflicts of interest

There are no conflicts to declare.

Acknowledgements

This work was supported by the Hyundai Motor group, by the Technology Development Program to Solve Climate Changes and by the Basic Science Research Program through the National Research Foundation of Korea (NRF) funded by the Ministry of Science, ICT & Future Planning (No. NRF-2017M1A2A2044501 and NRF-2018R1A2B6004996), and by the Materials and Components Technology Development Program of MOTIE/KEIT (10076731).

References

1 G. Jeong, Y.-U. Kim, H. Kim, Y.-J. Kim and H.-J. Sohn, *Energy Environ. Sci.*, 2011, **4**, 1986.
2 V. Etacheri, R. Marom, R. Elazari, G. Salitra and D. Aurbach, *Energy Environ. Sci.*, 2011, **4**, 3243.
3 P. Arora and Z. Zhang, *Chem. Rev.*, 2004, **104**, 4419.
4 Y. S. Jung, A. S. Cavanagh, L. Gedvilas, N. E. Widjonarko, I. D. Scott, S. H. Lee, G. H. Kim, S. M. George and A. C. Dillon, *Adv. Energy Mater.*, 2012, **2**, 1022.
5 D. Lin, Y. Liu and Y. Cui, *Nat. Nanotechnol.*, 2017, **12**, 194.
6 J. Janek and W. G. Zeier, *Nat. Energy*, 2016, **1**, 16141.
7 J. Qian, W. A. Henderson, W. Xu, P. Bhattacharya, M. Engelhard, O. Borodin and J.-G. Zhang, *Nat. Commun.*, 2015, **6**, 6362.
8 K. H. Park, Q. Bai, D. H. Kim, D. Y. Oh, Y. Zhu, Y. Mo and Y. S. Jung, *Adv. Energy Mater.*, 2018, **8**, 1800035.
9 Y. S. Jung, D. Y. Oh, Y. J. Nam and K. H. Park, *Isr. J. Chem.*, 2015, **55**, 472.
10 K. Kerman, A. Luntz, V. Viswanathan, Y.-M. Chiang and Z. Chen, *J. Electrochem. Soc.*, 2017, **164**, A1731.
11 X. Han, Y. Gong, K. K. Fu, X. He, G. T. Hitz, J. Dai, A. Pearse, B. Liu, H. Wang, G. Rubloff, Y. Mo, V. Thangadurai, E. D. Wachsman and L. Hu, *Nat. Mater.*, 2017, **16**, 572.
12 Y. Wang, W. D. Richards, S. P. Ong, L. J. Miara, J. C. Kim, Y. Mo and G. Ceder, *Nat. Mater.*, 2015, **14**, 1026.
13 S. Xin, Y. You, S. Wang, H. C. Gao, Y. X. Yin and Y. G. Guo, *ACS Energy Lett.*, 2017, **2**, 1385.
14 K. H. Park, D. Y. Oh, Y. E. Choi, Y. J. Nam, L. Han, J.-Y. Kim, H. Xin, F. Lin, S. M. Oh and Y. S. Jung, *Adv. Mater.*, 2016, **28**, 1874.
15 D. H. Kim, D. Y. Oh, K. H. Park, Y. E. Choi, Y. J. Nam, H. A. Lee, S.-M. Lee and Y. S. Jung, *Nano Lett.*, 2017, **17**, 3013.
16 Y. Yan, R.-S. Kühnel, A. Remhof, L. Duchêne, E. C. Reyes, D. Rentsch, Z. Łodziana and C. Battaglia, *Adv. Energy Mater.*, 2017, **7**, 1700294.
17 Y. Kato, S. Hori, T. Saito, K. Suzuki, M. Hirayama, A. Mitsui, M. Yonemura, H. Iba and R. Kanno, *Nat. Energy*, 2016, **1**, 16030.
18 N. Kamaya, K. Homma, Y. Yamakawa, M. Hirayama, R. Kanno, M. Yonemura, T. Kamiyama, Y. Kato, S. Hama, K. Kawamoto and A. Mitsui, *Nat. Mater.*, 2011, **10**, 682.
19 G. Sahu, Z. Lin, J. Li, Z. Liu, N. Dudney and C. Liang, *Energy Environ. Sci.*, 2014, **7**, 1053.
20 X. Yao, D. Liu, C. Wang, P. Long, G. Peng, Y.-S. Hu, H. Li, L. Chen and X. Xu, *Nano Lett.*, 2016, **16**, 7148.
21 C. Yu, S. Ganapathy, N. J. J. d. Klerk, I. Roslon, E. R. H. v. Eck, A. P. M. Kentgens and M. Wagemaker, *J. Am. Chem. Soc.*, 2016, **138**, 11192.
22 A. Hayashi, K. Noi, A. Sakuda and M. Tatsumisago, *Nat. Commun.*, 2012, **3**, 856.
23 A. Banerjee, K. H. Park, J. W. Heo, Y. J. Nam, C. K. Moon, S. M. Oh, S.-T. Hong and Y. S. Jung, *Angew. Chem., Int. Ed.*, 2016, **55**, 9634.

24 Z. Yu, S.-L. Shang, J.-H. Seo, D. Wang, X. Luo, Q. Huang, S. Chen, J. Lu, X. Li, Z.-K. Liu and D. Wang, *Adv. Mater.*, 2017, **29**, 1605561.

25 J. W. Heo, A. Banerjee, K. H. Park, S.-T. Hong and Y. S. Jung, *Adv. Energy Mater.*, 2018, **8**, 1702716.

26 D. P. Lu, Y. Y. Shao, T. Lozano, W. D. Bennett, G. L. Graff, B. Polzin, J. G. Zhang, M. H. Engelhard, N. T. Saenz, W. A. Henderson, P. Bhattacharya, J. Liu and J. Xiao, *Adv. Energy Mater.*, 2015, **5**, 1400993.

27 Y. D. Liu, Q. Liu, L. Xin, Y. Z. Liu, F. Yang, E. A. Stach and J. Xie, *Nat. Energy*, 2017, **2**, 17083.

28 B. R. Shin, Y. J. Nam, D. Y. Oh, D. H. Kim, J. W. Kim and Y. S. Jung, *Electrochim. Acta*, 2014, **146**, 395.

29 M. Nagao, A. Hayashi, M. Tatsumisago, T. Kanetsuku, T. Tsuda and S. Kuwabata, *Phys. Chem. Chem. Phys.*, 2013, **15**, 18600.

30 L. Porz, T. Swamy, B. W. Sheldon, D. Rettenwander, T. Frömling, H. L. Thaman, S. Berendts, R. Uecker, W. C. Carter and Y.-M. Chiang, *Adv. Energy Mater.*, 2017, **7**, 1701003.

31 P. Albertus, S. Babinec, S. Lizelman and A. Newman, *Nat. Energy*, 2018, **3**, 16–21.

32 E. J. Cheng, A. Sharafi and J. Sakamoto, *Electrochim. Acta*, 2017, **223**, 85–91.

33 Y. S. Jung, K. T. Lee, J. H. Kim, J. Y. Kwon and S. M. Oh, *Adv. Funct. Mater.*, 2008, **18**, 3010.

34 W. Zhang, D. A. Weber, H. Weigand, T. Arlt, I. Manke, D. Schröder, R. Koerver, T. Leichtweiss, P. Hartmann, W. G. Zeier and J. Janek, *ACS Appl. Mater. Interfaces*, 2017, **9**, 17835.

35 Y. S. Jung, P. Lu, A. S. Cavanagh, C. Ban, G. H. Kim, S. H. Lee, S. M. George, S. J. Harris and A. C. Dillon, *Adv. Energy Mater.*, 2013, **3**, 213.

36 A. Bhide, J. Hofmann, A. K. Durr, J. Janek and P. Adelhelm, *Phys. Chem. Chem. Phys.*, 2014, **16**, 1987.

37 X. Yu, J. B. Bates, G. E. Jellison and F. X. Hart, *J. Electrochem. Soc.*, 1997, **144**, 524.

38 Y. J. Nam, S.-J. Jo, D. Y. Oh, J. M. Im, S. Y. Kim, J. H. Song, Y. G. Lee, S.-Y. Lee and Y. S. Jung, *Nano Lett.*, 2015, **15**, 3317.

39 Y. J. Nam, D. Y. Oh, S. H. Jung and Y. S. Jung, *J. Power Sources*, 2018, **375**, 93.

40 Y. S. Jung, K. T. Lee, J. H. Ryu, D. Im and S. M. Oh, *J. Electrochem. Soc.*, 2005, **152**, A1452.

41 J. M. Whiteley, J. W. Kim, C. S. Kang, J. S. Cho, K. H. Oh and S.-H. Lee, *J. Electrochem. Soc.*, 2015, **162**, A711.

42 K. G. Gallagher, S. E. Trask, C. Bauer, T. Woehrle, S. F. Lux, M. Tschech, P. Lamp, B. J. Polzin, S. Ha, B. Long, Q. L. Wu, W. Q. Lu, D. W. Dees and A. N. Jansen, *J. Electrochem. Soc.*, 2016, **163**, A138.

43 P. Arora, M. Doyle and R. E. White, *J. Electrochem. Soc.*, 1999, **146**, 3543.

44 C. Uhlmann, J. Illig, M. Ender, R. Schuster and E. Ivers-Tiffee, *J. Power Sources*, 2015, **279**, 428.

45 L. E. Downie, L. J. Krause, J. C. Burns, L. D. Jensen, V. L. Chevrier and J. R. Dahn, *J. Electrochem. Soc.*, 2013, **160**, A588.

46 C. L. Tsai, V. Roddatis, C. V. Chandran, Q. L. Ma, S. Uhlenbruck, M. Bram, P. Heitjans and O. Guillon, *ACS Appl. Mater. Interfaces*, 2016, **8**, 10617.

47 R. Koerver, W. Zhang, L. d. Biasi, S. Schweidler, A. O. Kondrakov, S. Kolling, T. Brezesinski, P. Hartmann, W. G. Zeier and J. Janek, *Energy Environ. Sci.*, 2018, DOI: 10.1039/C8EE00907D.

48 K. R. Crompton and B. J. Landi, *Energy Environ. Sci.*, 2016, **9**, 2219.

49 P. Wang, P. Li, T.-F. Yi, H. Yu, X. Lin, S. Qian, Y.-R. Zhu, M. Shui and J. Shu, *Electrochim. Acta*, 2016, **190**, 248.

50 S. Wenzel, T. Leichtweiss, D. A. Weber, J. Sann, W. G. Zeier and J. Janek, *ACS Appl. Mater. Interfaces*, 2016, **8**, 28216.